Powder Technology 411 (2022) 117913

Contents lists available at ScienceDirect

Powder Technology

journal homepage: www.journals.elsevier.com/powder-technology

Numerical study of the effect of temperature and H_2O concentration on the electrostatic precipitator characteristics at high temperatures

Yongmin Shi [a], Mengxiang Fang [a,*], Qinhui Wang [a], Keping Yan [b], Jianmeng Cen [a], Weiqiang Zeng [a], Zhongyang Luo [a]

[a] State Key Lab of Clean Energy Utilization, Zhejiang University, Hangzhou 310027, China
[b] Coll Chem & Biol Engn, Inst Ind Ecol & Environm, Zhejiang University, Hangzhou 310028, China

HIGHLIGHTS

- A modified ESP model suitable for high temperature gas was established.
- The plasma model was used to simulate corona discharges in the ESP.
- The effect of temperature on ESP performance was studied numerically.
- The effect of H_2O concentration in flue gas on ESP performance was studied.

GRAPHICAL ABSTRACT

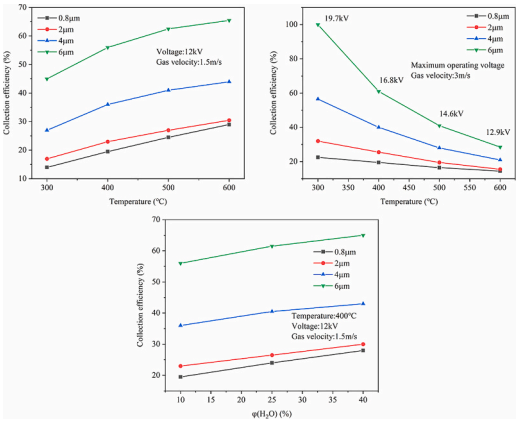

ARTICLE INFO

Keywords:
Electrostatic precipitator
High temperature
H_2O concentration
Electrical characteristics
Collection efficiency

ABSTRACT

In this study, a numerical model of an electrostatic precipitator (ESP) suitable for high-temperature flue gas was established using COMSOL Multiphysics, and the effects of temperature and H_2O concentration on the high-temperature ESP performance were studied. The results showed that, at the same voltage, increasing the temperature increased the negative ion density, thereby improving the particle charge and collection efficiency. However, increasing the temperature led to a decrease in the maximum operating voltage of the ESP, which reduced the negative ion density and electric field intensity at the maximum operating voltage and weakened the diffusion and field charges of the particles, leading to a further decrease in the maximum collection efficiency. Increasing the H_2O concentration in the flue gas increased the negative ion density and, thus, enhanced the diffusion charge of the particles, which helped improve the collection efficiency.

* Corresponding author.
E-mail address: mxfang@zju.edu.cn (M. Fang).

https://doi.org/10.1016/j.powtec.2022.117913
Received 21 June 2022; Received in revised form 30 August 2022; Accepted 2 September 2022
Available online 7 September 2022

Nomenclature

n_e	electron number density, $1/m^3$
Γ_e	electron flux, $1/m^2 \cdot s$
R_e	source term of electron, $1/(m^3 \cdot s)$
E	electric field intensity, V/m
μ_e	electron mobility, $m^2/(V \cdot s)$
D_e	electron diffusion coefficient, m^2/s
e	electronic charge
n_ε	electron energy density, eV/m^3
D_ε	electron energy diffusion coefficient, m^2/s
R_ε	energy loss/gain due to inelastic collisions, $eV/(m^3 \cdot s)$
μ_ε	electron energy mobility, $m^2(eV \cdot s)$
T_e	electron temperature, eV
x_j	mole fraction of the target species for reaction j
k_j	rate coefficient for reaction j, m^3/s
$\Delta\varepsilon_j$	energy loss for reaction j, eV
N_n	total neutral number density, $1/m^3$
m_e	electron mass, kg
σ_j	collision cross section, m^2
f	electron energy distribution function (EEDF)
ε	electron energy, eV
w_k	mass fraction of species k
u	fluid velocity vector, m/s
j_k	diffusive flux
R_k	rate expression
ρ	density of the mixture, $1/m^3$
V_k	multi-component diffusion coefficient of species k, m^2/s
D_k	diffusion coefficient of species k, m^2/s
M_n	mean molecular mass
T	gas temperature, K
D_k^T	thermal diffusion coefficient of species k, m^2/s
z_k	charge of species k, C
μ_k	mobility of species k, $m^2/(V \cdot s)$
n_k	number density of species k, $1/m^3$
Γ_k	flux density of species k, $1/(m^2 \cdot s)$
q_i	ion charge, C
m_g	gas molecular mass, kg
d_i	ion diameter, m
P	absolute pressure, Pa
k_B	Boltzmann constant
ε_0	permittivity of free space
ε_r	relative permittivity
n_p、n_n	number density of positive and negative ions, respectively, $1/m^3$
V	potential, V
n	boundary normal vector
γ_p	secondary electron emission coefficient
Γ_p	secondary emission electron flux, $1/(m^2 \cdot s)$
ρ_{gas}	gas density, kg/m^3
μ_{gas}	effective gas viscosity, $kg/(m \cdot s)$
ρ_{ion}	ion space charge density, C/m^3
u_{gas}	gas velocity, m/s
M_{gas}	mean molecular mass of the flue gas
R_M	gas constants, R_M=8.314 J/mol·K
r_i	molar fraction of each gas in the mixture
μ_i	viscosity of each gas in the mixture, $kg/(m \cdot s)$
g_i	mass fraction of each gas in the mixture
M_i	relative molecular mass of each gas in the mixture
q_s、q_p	saturation particle charge, and particle charge C
τ	time constant
d_p	particle diameter, m
Z_{ion}	total flue gas ion mobility, $m^2/(V \cdot s)$
Z_i	ion mobility of each gas in the mixture, $m^2/(V \cdot s)$
Z_{i0}	ion mobility of each gas in the mixture under standard conditions, $m^2/(V \cdot s)$
u_p	particle velocity, m/s
ρ_p	particle density, kg/m^3
C_d	drag coefficient
Re	Reynolds number
C_c	Cunningham correction factor
λ	mean free path, m
$\varphi(i)$	volume fraction of each gas in the mixture
U_j	breakdown voltage, kV
d	electrode spacing, mm
δ	relative gas density

1. Introduction

As the emission standards for flue gas pollutants in key industrial fields, such as the cement, glass, iron and steel, and petrochemicals fields, are gradually becoming stricter; stricter requirements are being set for reducing the emission of industrial flue gas pollutant. Many industries need to de-dust high-temperature dusty flue gas in process systems to achieve high-temperature flue gas purification [1]. An electrostatic precipitator (ESP) is an effective technology used to remove particles at high temperatures and has great market prospects in various industries owing to its low pressure drop, high efficiency, and wide range of adaptability [2–4]. Computational fluid dynamics is a powerful tool for studying corona discharge and particle-trapping processes in ESPs [5]. The following three basic physical processes occur in an ESP: corona discharge, gas flow, and particle migration [6]. Corona discharge is a major factor affecting particle removal. The electric field distribution and space charge density distribution directly affect particle charging and migration [7].

Corona discharge is very important in ESP simulations because it is the basis for particle charging. In most previous numerical studies, a simplified corona discharge model was used, termed the single-species stationary model [5]. In this model, the ionization layer was neglected and the steady-state flow of one ionic species was considered. The formulation of the boundary conditions, which is essential for calculating the space charge in the discharge region, is crucial in this model. The most natural method is to use an experimentally measured corona current, which also removes many secondary factors that affect the accuracy of the simulation [8]. Another simpler solution is to adopt Kaptzov's assumption that the electric field on the surface of the corona electrode is a constant value calculated using Peek's formula [9]. Many numerical studies on ESPs have been conducted based on this model. For example, Luo et al. [10] developed an integrated model based on this discharge model to study the effect of temperature on corona discharge. Zheng et al. [7] and Yang et al. [11] considered the effect of dust particle charge using this discharge model, and they investigated the effect of particle charge on the electric field and space charge density. Zhang et al. [12] added a dust layer discharge model to this discharge model and found that the dust layer reduced the electric field intensity and particle charge. In addition, numerous numerical studies on the structural parameters of the ESPs based on this discharge model have been performed [13–18]. Most of these numerical studies used the parameters of air for calculation, and there are few studies that adopted complex atmospheres and gas components. However, ESPs are often operated in flue gases with complex gas compositions, including N_2, O_2, CO_2, H_2O, CO, NO_x, and SO_x. Flue gas components change with different fuels and operating conditions, and many experimental studies have explored the influence of flue gas components on the discharge characteristics [19–22], but few numerical studies exist in this area. In addition, current

numerical studies mainly focus on conventional ESPs (<200 °C), while some industries, such as the metallurgy and cement industries, are required to perform dust removal in high-temperature flue gas (>350 °C). More importantly, it has been shown that during high-temperature gas discharge, the actual corona onset electric field is significantly lower than the value calculated using Peek's formula, and the electron current in the high-temperature discharge current cannot be neglected; therefore, the conventional model is not applicable to corona discharge at high temperatures [23–24].

In this study, we first established an ESP model suitable for high-temperature gases using COMSOL Multiphysics. We adopted a plasma model to simulate corona discharge and coupled it with the flow field and particle transport. The model was then used to explore the effects of temperature and H_2O concentration in the flue gas on the distribution of charge carriers, discharge the current, electrical characteristics, and the collection efficiency.

2. Numerical methods

2.1. Basic physical process

In an ESP, the dust removal process primarily involves three physical fields, namely the electric field, flow field, and particle transport. All of these are mutually coupled, although some couplings are weaker than others and can be neglected. Studies have shown that, for a low-concentration dust-laden airflow, the effect of particles on the space charge can be ignored during the calculation process. In addition, the electric field can affect the flow field through the ionic wind, whereas the opposite coupling reaction is weak and can be neglected [5]. Therefore, the influences of the particle and flow fields on the electric field were ignored in this study. A schematic of the multiphysics field coupling is shown in Fig. 1.

2.2. Corona discharge model

2.2.1. Negative corona discharge process

During the negative corona discharge process, the discharge space can be divided into the corona and drift regions, and the corona region can be further divided into the ionization and attachment regions [23]. Most types of particles exist in the corona region, including electrons, positive and negative ions, and gas molecules. When a voltage is applied, positive ions migrate in the direction of the electric field lines, whereas electrons and negative ions migrate in the direction opposite to the electric field lines. These free charges collide with gas molecules during the migration process, and various discharge reactions occur, including ionization, attachment, dissociation, excitation, and charge transfer. In our simulation, the flue gas comprised N_2, CO_2, O_2, and H_2O. We used the plasma model to determine the electric field characteristics, without ignoring ion diffusion and electron density, and considered the kinetics of discharge chemical reactions, including the ionization reaction, attachment reaction, and positive and negative ion-recombination reactions. The species included electrons (e), negative ions (O^-, O_2^-, CO_3^-, CO_4^-, and OH^-), positive ions (N_2^+, O_2^+, N_4^+, O_4^+, $N_2O_2^+$, H_2O^+, CO_2^+, and CO^+), and neutral atoms (N_2, O_2, CO_2, H_2O, O, O_3, H, H_2, C, CO, and OH). In addition, 50 discharge chemical reactions were considered in the model (as shown in Supplementary Material) [25–29].

2.2.2. Plasma model

The governing equations of the fluid dynamics model are usually composed of the electron continuity equation, positive and negative ion continuity equations, electron energy conservation equation, and Poisson equation. The electron density and average electron energy in the model are calculated using the following continuity equations:

$$\frac{\partial}{\partial t}(n_e) + \nabla \bullet \Gamma_e = R_e \tag{1}$$

$$\frac{\partial}{\partial t}(n_\varepsilon) + \nabla \bullet [-n_\varepsilon(\mu_\varepsilon \bullet E) - D_\varepsilon \bullet \nabla n_\varepsilon] + E \bullet \Gamma_e = R_\varepsilon \tag{2}$$

$$\Gamma_e = -n_e(\mu_e \bullet E) - D_e \bullet \nabla n_e \tag{3}$$

D_e, μ_ε, and D_ε were calculated from the electron mobility μ_e using the following formula:

$$D_e = \mu_e T_e \tag{4}$$

$$\mu_\varepsilon = \frac{5}{3}\mu_e \tag{5}$$

$$D_\varepsilon = \mu_\varepsilon T_e \tag{6}$$

The source terms R_e and R_ε were determined based on the plasma

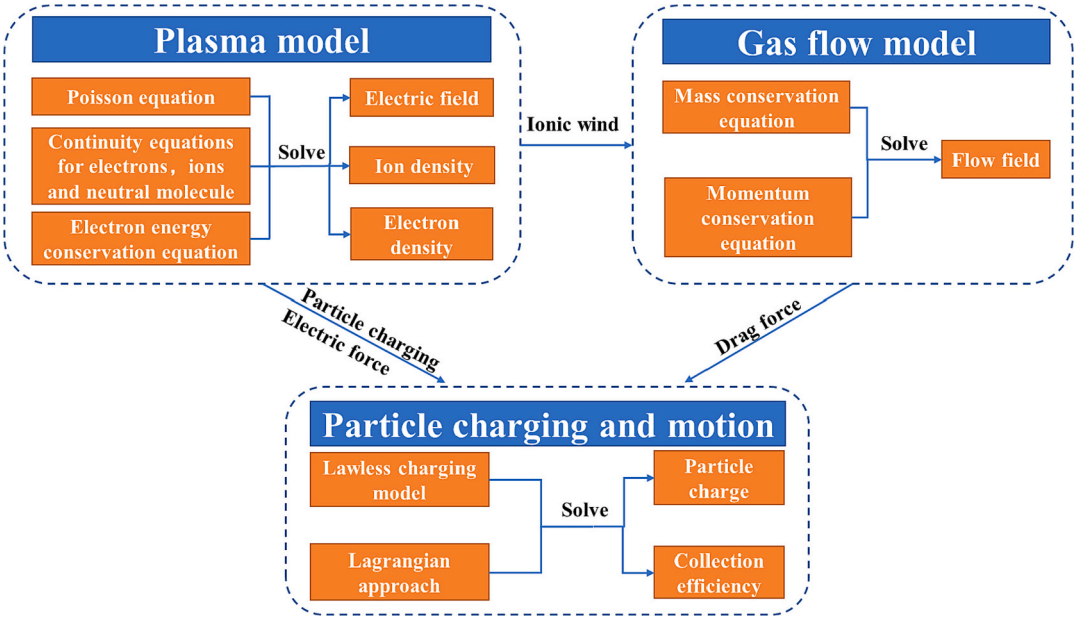

Fig. 1. Multiphysics field coupling schematic.

chemistry using the rate coefficients calculated as follows:

$$R_e = \sum_{j=1}^{M} x_j k_j N_n n_e \tag{7}$$

$$R_e = \sum_{j=1}^{M} x_j k_j N_n n_e \Delta\varepsilon_j \tag{8}$$

The rate coefficient k_j was computed from the cross section using the following equation:

$$k_j = \gamma \int_0^{\infty} \varepsilon\sigma_j(\varepsilon) f(\varepsilon) d\varepsilon \tag{9}$$

$$\gamma = \sqrt{\frac{2e}{m_e}} \tag{10}$$

where σ_j is the collision cross-section taken from the Lxcat database [25] and f is the electron energy distribution function.

Heavy particles, such as ions, atoms, and molecules, can be described using the continuity equation as follows:

$$\rho\frac{\partial}{\partial t}(w_k) + \rho(u \bullet \nabla)w_k = \nabla \bullet j_k + R_k \tag{11}$$

j_k is the diffusive flux and is expressed as follows:

$$j_k = \rho w_k V_k \tag{12}$$

V_k is the multi-component diffusion coefficient of species k. According to the mixture average model, this can be expressed as following:

$$V_k = D_k\frac{\nabla w_k}{w_k} + D_k\frac{\nabla M_n}{M_n} + D_k^T\frac{\nabla T}{T} - z_k\mu_k E \tag{13}$$

Because a variety of ions must be considered in the plasma model, the ion mobility of each ion at different temperatures was calculated using the Friedlander formula as follows [30]:

$$\mu_k = 0.441 \bullet q_i \left(\frac{\sqrt{k_B \bullet T/m_g}}{P \bullet {d_i}^2}\right) \tag{14}$$

The electrostatic field was calculated using the following Poisson's equation:

$$-\nabla \bullet \varepsilon_0\varepsilon_r\nabla V = e\left(\sum n_p - n_e - \sum n_n\right) \tag{15}$$

$$E = -\nabla V \tag{16}$$

The boundary conditions for corona discharge must consider the reactions that occur after the collision of charged particles with the electrode, such as reflection and secondary electron emission. The boundary conditions of the electron transport equation at the electrodes can be expressed as follows:

$$n \bullet \Gamma_e = \left(\frac{1}{2}\sqrt{\frac{8k_B T_e}{\pi m_e}} n_e\right) - \sum_p \gamma_p(\Gamma_p \bullet n) \tag{17}$$

These ions become stable gas molecules at the electrode. The electrode boundary conditions of the ions and neutral molecules can be expressed by the following formula:

$$n \bullet \Gamma_k = \left(\frac{1}{4}\sqrt{\frac{8k_B T}{\pi m_k}} n_k\right) \tag{18}$$

2.3. Flow field model

The flow field in the ESP is calculated using the time-averaged Navier–Stokes equation together with the RNG k–ε turbulence model. In an industrial ESP, the gas flow is typically considered as an incompressible, viscous, steady-state flow and can be described by the following equations:

Conservation of mass:

$$\nabla(\rho_{gas} u_{gas}) = 0 \tag{19}$$

Conservation of momentum:

$$\rho_{gas}\left(\frac{\partial u}{\partial t} + u_{gas} \bullet \nabla u_{gas}\right) = -\nabla P + \mu_{gas}\nabla^2 u_{gas} + \rho_{ion} E \tag{20}$$

where the term $\rho_{ion}E$ represents the ionic wind effect on the main flow.

In this study, flue gas was regarded as a mixture of ideal gases. The density and dynamic viscosity of the gas are affected by temperature and were calculated using the following equations:

Density of flue gas:

$$\rho_{gas} = \frac{PM_{gas}}{R_M T} \tag{21}$$

$$M_{gas} = 28.062 r_{N_2} + 44.01 r_{CO_2} + 32 r_{O_2} + 18.016 r_{H_2O} \tag{22}$$

Dynamic viscosity of flue gas at different temperatures [31]:

$$\mu_{N_2} = \frac{1.0385 \times 10^{-2}}{T + 118}\left(\frac{T}{373}\right)^{1.5} \tag{23}$$

$$\mu_{CO_2} = \frac{1.1394 \times 10^{-2}}{T + 252}\left(\frac{T}{373}\right)^{1.5} \tag{24}$$

$$\mu_{O_2} = \frac{1.2622 \times 10^{-2}}{T + 138}\left(\frac{T}{373}\right)^{1.5} \tag{25}$$

$$\mu_{H_2O} = \frac{1.8875 \times 10^{-2}}{T + 1191}\left(\frac{T}{373}\right)^{1.5} \tag{26}$$

$$\mu_{gas} = \sum_i g_i \mu_i \tag{27}$$

$$g_i = r_i\frac{M_i}{M_{gas}} \tag{28}$$

The above formula has an error of <2% within 0–1000 °C.

2.4. Particle charging model

Particle charging occurs when the particles move in the corona field. The charging mechanism is divided into electric field charging and diffusion charging. The combined charge model proposed by Lawless [32] can accurately calculate the charging number and rate, which can be described as follows:

$$\frac{dq_p}{dt} = \begin{cases} \frac{q_s}{\tau}\left(1 - \frac{q}{q_s}\right)^2 + \frac{2\pi\alpha\rho_{ion}Z_{ion}k_B d_p}{e} & q \le q_s \\ \frac{\alpha}{4\tau}(q - q_s)exp\left(\frac{e(q - q_s)}{2\pi\varepsilon_0 Z_{ion}k_B T d_p}\right) & q > q_s \end{cases} \tag{29}$$

$$\alpha = \begin{cases} 1 & e_{norm} < 0.525 \\ \frac{1}{(e_{norm} + 0.457)^{0.575}} & e_{norm} > 0.525 \end{cases} \tag{30}$$

$$e_{norm} = \frac{e d_p}{2k_B T}E \tag{31}$$

In the particle-charging model, the ion mobility is influenced by the temperature and gas composition. Considering that a variety of ions are involved in the plasma model, it is difficult to calculate the total ion mobility of flue gas using the Friedlander formula. To simplify the calculation process, the ion mobility at different temperatures in the particle charging model was calculated using the following formula

[33]:

$$\frac{1}{Z_{ion}} = \sum_i \frac{r_i}{Z_i} \tag{32}$$

$$Z_i = Z_{i0} \bullet \left(\frac{T}{T_0}\right) \tag{33}$$

where Z_i is the ion mobility of component i , Z_{i0} is the ion mobility of component i under standard conditions, and $T_0 = 273.15K$. The ion mobilities of the different gases under standard conditions are listed in Table 1.

2.5. Particle transport model

The motion of particles is mainly affected by the drag force, gravity, and electric force in an ESP. Therefore, the Lagrangian approach was adopted to calculate the particle motion before its escape or capture. The particle motion equation can be described as follows:

$$m_p \frac{du_p}{dt} = \frac{1}{8}\pi C_d \rho_{gas} d_p^2 |u_{gas} - u_p|(u_{gas} - u_p) + Eq_p + m_p g \frac{\rho_p - \rho_{gas}}{\rho_p} \tag{34}$$

$$C_d = \begin{cases} \dfrac{24}{Re} \; Re < 0.1 \\ \dfrac{22.73}{Re} + \dfrac{0.0903}{Re^2} + 3.69 \; 0.1 < Re < 1 \end{cases} \tag{35}$$

$$Re = \frac{\rho_{gas}|u_p - u_{gas}|d_p}{\mu_{gas}} \tag{36}$$

$$C_c = 1 + \frac{2\lambda}{d_p}\left(1.257 + 0.4exp\left(-\frac{1.1d_p}{2\lambda}\right)\right) \tag{37}$$

The terms on the right-hand side of Eq. (34) denote the drag force, electric force, and gravitational force, respectively.

Collection efficiency η was calculated by the following equation:

$$\eta = \frac{m_{in} - m_{out}}{m_{in}} \times 100\% \tag{38}$$

where m_{in} is the inlet mass concentration of particles (g/Nm^3) and m_{out} is the outlet mass concentration of particles (g/Nm^3).

2.6. Model conditions and calculation procedure

In this study, a wire-cylinder ESP was configured for model development. All numerical calculations were performed using COMSOL Multiphysics. A plasma module was used to solve the electric field. A computational fluid dynamics module was utilized for the gas flow field. A particle tracking module was applied for particle transport. The geometric structure and grid divisions are shown in Fig. 2. To simplify the calculation process and considering the symmetry of the model, the plane region on the axisymmetric side was selected as the computational control domain. The entire geometry was discretized using an unstructured mesh, and refined grids were applied around the electrodes to improve the modeling accuracy. The geometry and operating parameters of the ESP are presented in Table 2. The gas components are listed in Table 3. The following procedure was executed for the simulation. First, the electric field and charge density distribution at the moment of discharge stabilization were obtained by solving the plasma model, and the calculated electric field and charge distribution were used as the given conditions to perform the coupling calculation of the electric and flow fields to obtain the flow field characteristics. Finally, the particles were injected into the computational domain and the particle charge equation, and the equation of motion was solved to obtain the particle transport characteristics. The boundary conditions used for the calculations are listed in Table 4.

Table 1
Ion mobility of different gases under standard conditions.

Component	Negative ion mobility, m^2/V·s	Positive ion mobility, m^2/(V·s)
N_2	–	1.8×10^{-4}
CO_2	9.8×10^{-5}	8.4×10^{-5}
O_2	2.6×10^{-4}	2.2×10^{-4}
H_2O	9.5×10^{-5}	1.1×10^{-4}

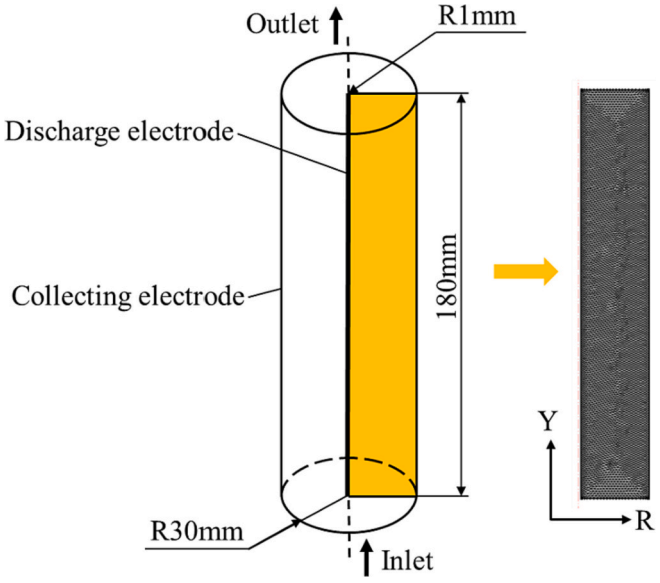

Fig. 2. ESP geometry model and computational meshes.

Table 2
Geometric and operating parameters.

Parameter, unit	Value	Parameter, unit	Value
Length, m	0.18	Pressure, atm	1
Temperature, °C	300–600 °C	Applied voltage, kV	−8-18
Gas velocity, m/s	1.5 , 3	Particle density, kg/m^3	2200
Wire radius, mm	1	Particle diameter, μm	0.8, 2, 4, 6
Cylinder radius, mm	30		

Table 3
Flue gas components.

Group	Flue gas components (%)			
	φ(N_2)	φ(CO_2)	φ(O_2)	φ(H_2O)
1	70	8	12	10
2	55	8	12	25
3	40	8	12	40

Table 4
Boundary conditions.

	Electric potential	Electron	Ion	Gas flow	Particle motion
Discharge electrode	$V = V_0$	Eq. (17)	Eq. (18)	Non-slip	Reflect
Collecting electrode	$V = 0$	Eq. (17)	Eq. (18)	Non-slip	Trap
Inlet	$-n \bullet \nabla \varepsilon_0\varepsilon_r E = 0$	$-n \bullet \Gamma_e = 0$	$-n \bullet \Gamma_k = 0$	Velocity	Escape
Outlet	$-n \bullet \nabla \varepsilon_0\varepsilon_r E = 0$	$n \bullet \Gamma_e = 0$	$-n \bullet \Gamma_k = 0$	Pressure	Escape

3. Results and discussion

3.1. Model validation

3.1.1. Verification of discharge current results

To verify the accuracy of the model, we conducted experiments and simulations at different temperatures and H_2O concentrations and compared the experimental V—I curves with the simulated results. To ensure relevance, the model parameters were kept consistent with the experimental parameters. The experimental setup is shown in Fig. 3. The effective length of the discharge electrode was 180 mm, the diameter was 2 mm, and the heteropolar distance of the discharge device was 29 mm. H_2O was injected into the pipeline using a syringe pump. A heating coil was wrapped around the pipeline between the syringe pump and inlet port to ensure that the H_2O evaporated quickly and mixed with the gas after entering the pipeline. The H_2O concentration was controlled by controlling the injection speed of the syringe pump. The results are shown in Fig. 4. The simulated results were consistent with the experimental data. Considering the measurement errors of the experimental instruments, the model exhibited high accuracy in predicting the high-temperature discharge characteristics in the range of the working conditions measured in this study.

3.1.2. Validation of collection efficiency results

To further verify the accuracy of the model, we compared the experimentally obtained collection efficiency with the simulation results. Experimental data were derived from our previous study [34]. The dust removal experimental device is shown in Fig. 5, where the effective length of the ESP was 1.2 m, radius of the discharge electrode was 1 mm, and radius of the dust collection electrode was 50 mm. In the experiment, the gas velocity was 0.12 m/s, and the discharge atmosphere was air (gas in the numerical calculation: $\varphi(N_2) = 78.94\%$, $\varphi(O_2) = 21\%$, $\varphi(CO_2) = 0.03\%$, $\varphi(H_2O) = 0.03\%$). A dust sampling port was placed at the outlet of the ESP. The particle concentrations were sampled using a PM10 impactor and measured using an electronic balance. The particle concentration, measured at an applied voltage of 0 kV, was used as the inlet dust concentration. The dust collection efficiency was calculated using Eq. (38). We performed numerical calculations based on experimental parameters to verify the accuracy of the collection efficiency calculated in the model. The total collection efficiency of the numerical model was obtained using Eq. (39), where n_{di} is the volume weight of particles with diameter of di and η_{di} is the collection efficiency of particles with diameter of di. The particle size distribution was obtained from reference [34] (Fig. 6). A comparison between the experimental and calculated values for dust collection efficiency is shown in Fig. 7. The calculated results were lower than the experimental results at low voltages, but very close at high voltages. At low voltages, the particles were not completely collected; during the experiment, the particles had an agglomeration effect, and the small particles agglomerated into large particles, thereby increasing the particle charge and improving the dust removal efficiency. The agglomeration between particles was not considered in the simulation calculation; thus, the calculated value was small. When the voltage was larger (>12 kV), the calculated value reached 100%, which meant that the particles were completely collected. However, in the experimental process, the collection efficiency could not reach 100% owing to the presence of the secondary dust effect; consequently, the experimental value was very close to 100%, but slightly lower than 100%. Therefore, the calculated value at low voltage was lower than the experimental value, whereas at high voltages, they were very close to each other. However, in general, the simulation results were consistent with the experimental results.

$$\eta = \sum_{i=0}^{i=\infty} n_{di}\eta_{di} \tag{39}$$

3.2. Distributions of charge carrier number density

The 2D and radial distributions of the charge carrier density are presented in Fig. 8 (Y position = 90 mm). In the region from the discharge electrode to the anode, the electron density first increased and reached a maximum at the ionization boundary and then decreased rapidly. Positive ions were concentrated around the discharge electrode with an order of magnitude of 10^{15}, which was much larger than that of the electrons and negative ions. The positive ion density decreased rapidly with increasing distance from the discharge electrode. The negative ion density first increased and then decreased with increasing distance from the discharge electrode. Negative ions were the main charge carriers in the drift region, and their number density in the drift region was several orders of magnitude higher than that of the positive ions and electrons. This charge carrier distribution was mainly caused by the different electric field forces acting on the different charge carriers in the discharge region. Owing to the negative voltage applied to the discharge electrode, the electric field was directed from the ground electrode to the discharge electrode. Ionization and attachment reactions occurred in the corona region, and the resulting positive ions migrated toward the discharge electrode under the electric field force, while the negative ions rapidly entered the drift region. Therefore, the density of positive ions was higher in the region near the discharge electrode, whereas negative ions were mainly present in the drift zone. During the operation of an ESP, particles are charged mainly by collisions with negative ions and then removed by the electric field force.

3.3. Composition of corona current at high temperature

The composition of corona currents has been studied by several researchers. Goldman et al. [35] found a saturation amount of unipolar ion

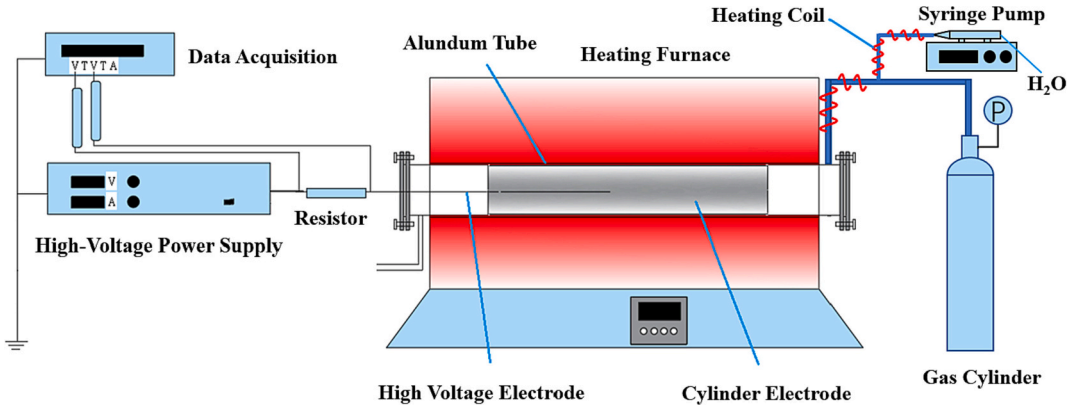

Fig. 3. Discharge experimental setup.

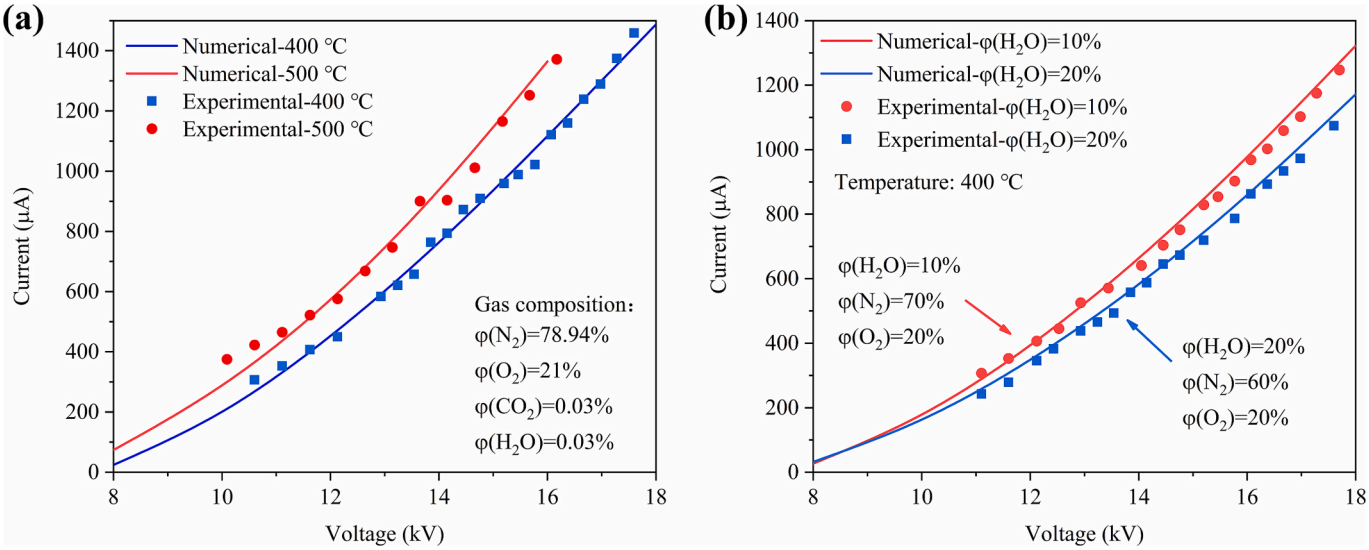

Fig. 4. Comparison of discharge characteristics curves between computational results and experimental data at different (a) temperatures and (b) H_2O concentrations.

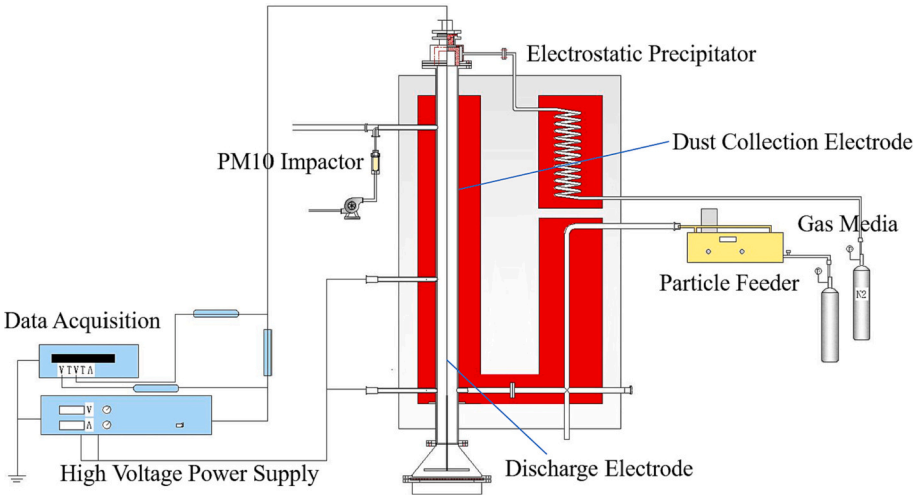

Fig. 5. Schematic of the experimental setup.

concentration near a ground electrode. Sigmond et al. [36] derived an equation for the saturation ion density using theoretical derivation, which led to the saturation ion current density equation being obtained. Yan [37] and Xiao [24] conducted discharge experiments at high temperatures and found that the total current at high temperatures and voltages was always higher than the calculated saturation ion current, proving that the electron current at high temperatures cannot be neglected. However, because the electron current in the corona current cannot be measured directly, researchers often obtain the electron current by solving for the difference between the total current and saturation ion current. When the total current was less than the saturation ion current, they considered that there was no electron current [37]. However, Sigmond found that an electron current was also likely to exist in the corona current below the saturation ion current [36]. In this study, a plasma model was used to calculate corona discharge. The electron and ion current densities was obtained, and the total corona current density is the sum of both. The variation curves of the total discharge and ion currents at 400 °C are shown in Fig. 9. The saturation ion current density was calculated using Eq. (40) [36]. Both the ion current and the total current increased with increasing voltage. The ion current density was always significantly lower than the total corona current density, proving that the electron current cannot be neglected at high temperatures and that the electron current is also present in the corona current below the saturation ion current. In addition, the gap between the ion current and the saturation ion current gradually decreased as the voltage increased. The ion current reached saturation at 18 kV. Therefore, conventional corona discharge models that tend to ignore electrons are not applicable to modeling corona discharges at high temperatures. When an ESP is operated, the dust particles are charged by colliding with ions, the ion current is useful for the ESP to remove dust, and the electron current has a minor contribution to dust removal but greatly increases the energy consumption of the precipitator [38].

$$I_s = \frac{2\pi\varepsilon_0 Z_{ion} V^2}{R^2} \tag{40}$$

3.4. Characteristics of electric field

3.4.1. Effect of temperature

The temperature had a significant influence on the performance of the high-temperature ESP. In particular, high temperatures led to a drop in the breakdown voltage, which in turn had an impact on the collection

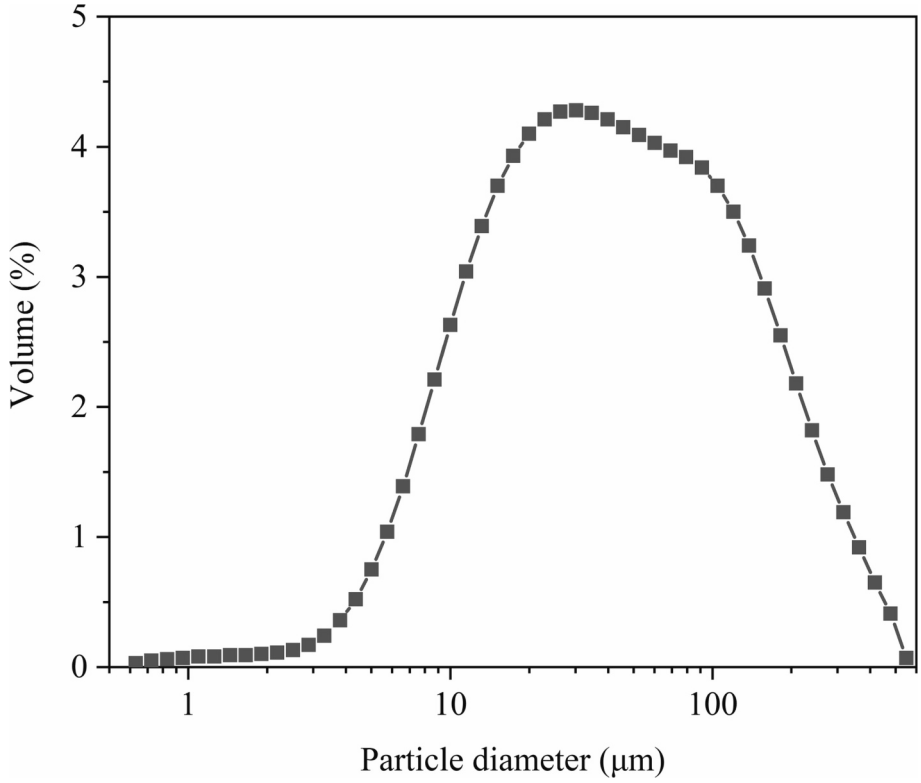

Fig. 6. Particle size distribution.

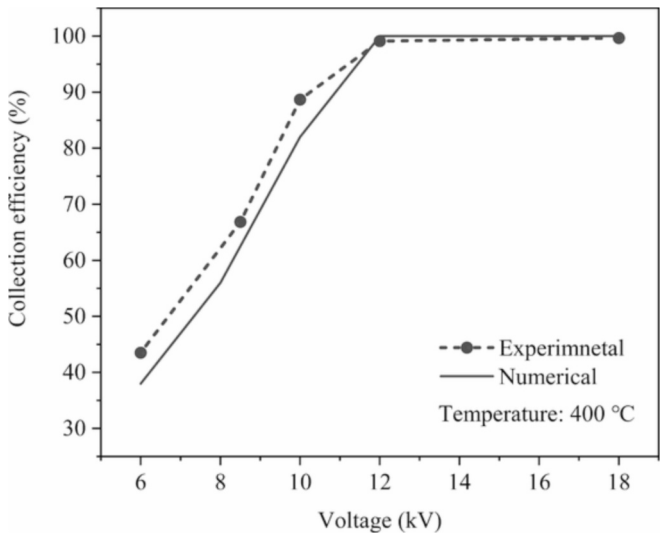

Fig. 7. Comparison of collection efficiency between computational results and experimental data in the ESP.

efficiency. Therefore, when studying the effect of temperature on the performance of ESPs, it is important to consider not only the temperature as a variable but also decreases in the breakdown voltage due to temperature rise. To fully investigate the effect of temperature on the ESP performance, this section investigates and compares the effect of temperature on the electric field characteristics at the same voltage and at the maximum operating voltage. The maximum operating voltage was defined as the maximum voltage that could enable the ESP to operate stably at a given temperature, and it varied with temperature. In actual industries, when the applied voltage is close to the breakdown voltage, the operation of an ESP becomes unstable; therefore, a voltage slightly below the breakdown voltage is often used as the maximum operating voltage. For convenience, 0.95 times the breakdown voltage was used as the maximum operating voltage. The breakdown voltage was calculated using Eq. (41) [39–40]. The maximum operating voltage decreased with increasing temperature (Table 5). In addition, the gas component used for the calculation was group 1.

The effect of temperature on the radial distribution of the negative ion density at the same voltage and maximum operating voltage is shown in Fig. 10(a). As can be seen from the figure, at the same voltage, the negative ion density increased with increasing temperature, whereas at the maximum operating voltage, the effect of temperature on the negative ion density was the opposite of that at the same voltage, and the negative ion density decreased with increasing temperature. The effect of temperature on the radial distribution of the electric field intensity at the same voltage and maximum operating voltage is shown in Fig. 10(b). At the same voltage, the electric field intensity distribution generally varied less with the temperature change. In the region near the discharge electrode, the electric-field intensity decreased with increasing temperature, whereas it increased with increasing temperature near the grounding electrode. At the maximum operating voltage, the electric field intensity distribution curve shifted downward with increasing temperature on average, and the electric field intensity decreased with increasing temperature in all discharge regions. In addition, the electric field intensity on the surface of the discharge electrode decreased with increasing temperature. At a voltage of 12 kV, the electric field intensity on the surface of the discharge electrode decreased from 2.9×10^6 V/m to 2.15×10^6 V/m when the temperature increased from 300 °C to 600 °C.

$$U_j = 1.5 \times 10^6 d\delta \tag{41}$$

3.4.2. *Effect of H_2O concentration*

Gas components have an important effect on corona discharge characteristics, and the effect of H_2O concentration in high-temperature flue gas components on the electric field characteristics is explored in

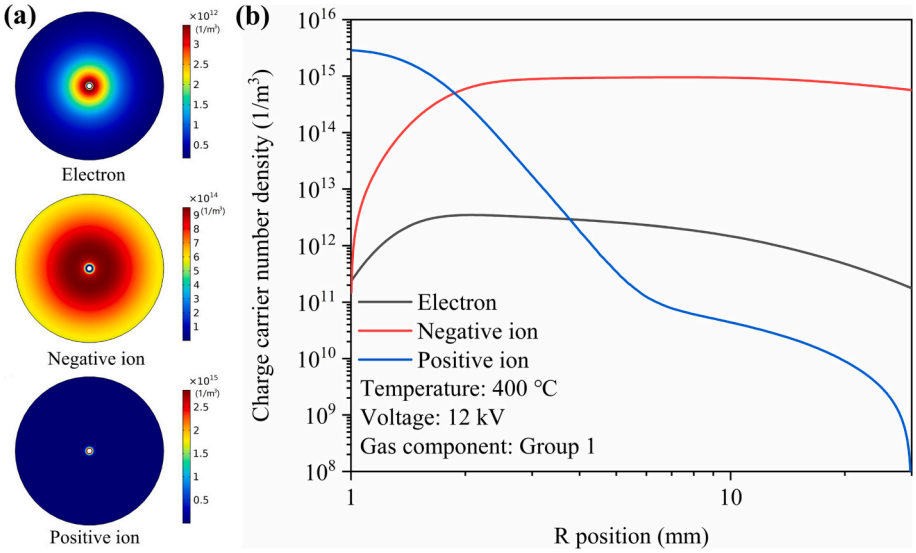

Fig. 8. Charge carrier number density distribution: (a) 2D distribution, (b) radial distribution (temperature: 400 °C, voltage: 12 kV).

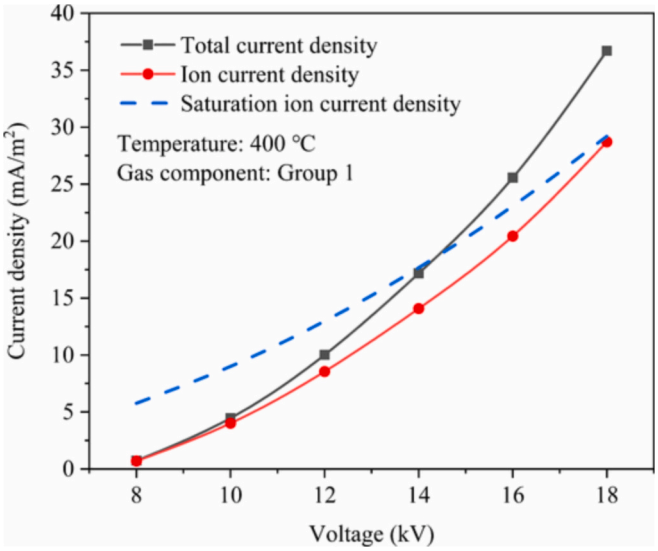

Fig. 9. Total current density distribution and ion current density distribution.

Table 5
Maximum operating voltage at different temperatures.

Temperature, °C	300	400	500	600
Operating voltage, kV	19.7	16.8	14.6	12.9

this section. The gas temperature used in the simulation was maintained at 400 °C. Fig. 11 shows the effect of H_2O concentration on the distribution of the negative ion number density and electric field intensity at an applied voltage of 12 kV. When the gas temperature and voltage were constant, the negative-ion number density increased with increasing H_2O concentration. H_2O is a strong electronegative gas, and increasing the concentration of H_2O in the gas enhanced the overall electronegativity of the high-temperature flue gas and improved the ability of gas molecules to attach electrons, thereby increasing the density of the negative ions, which is conducive to particle charging. Fig. 11(b) illustrates the distribution of the electric field intensity for different H_2O volume fractions. The overall electric-field intensity distribution was less affected by the H_2O concentration. When the H_2O concentration increased, the electric-field intensity decreased in the area near the discharge electrode and increased in the area near the grounding electrode. The effect of H_2O concentration at different voltages on the electric field intensity at the surface of the discharge electrode is shown in Fig. 12. As can be seen from the figure, the electric field intensity on the surface of the discharge electrode decreased with increasing of H_2O concentration, indicating that increasing the H_2O concentration can reduce the corona onset voltage. In addition, it is worth noting that the discharge electrode surface electric field increased with increasing voltage, indicating that the change in voltage also had an effect on the discharge electrode surface electric field. Therefore, it was unreasonable for the conventional corona discharge model to use the constant value calculated using Peek's formula as the discharge electrode surface electric field.

3.5. Dust removal characteristics

3.5.1. Effect of temperature

Temperature influences particle charging and removal by affecting the electric field characteristics. This section further explores the effect of temperature on particle charge and collection efficiency at the same voltage and maximum operating voltage. The collection efficiency achieved by the ESP at the maximum operating voltage was its maximum collection efficiency at a given temperature.

Fig. 13 illustrates the charge number of particles with diameter of 0.8, 2, 4, and 6 μm at different temperatures under the same and maximum operating voltages. The charges of large particles were greater than those of small particles. At the same voltage, increases in temperature increased the density of negative ions; thus, the particle charge increased with increasing temperature. However, at the maximum operating voltage, the effect of the temperature change on the charge number of particles with different diameters was different. At the maximum operating voltage, the particle charge decreased with increasing temperature for 2, 4, and 6 μm particles, while it increased with increasing temperature for 0.8 μm particles. There are two main mechanisms for particle charging: field charging and diffusion charging. Large particles are mainly affected by the electric field charge and can reach saturation within a short time after entering an ESP. The saturation field charge was only related to the electric field intensity, which decreased with increasing temperature at the maximum operating voltage; therefore, the charge of large particles also decreased with increasing temperature. For small particles, the effect of the diffusion charge is greater, the diffusion charge is related to the negative ion

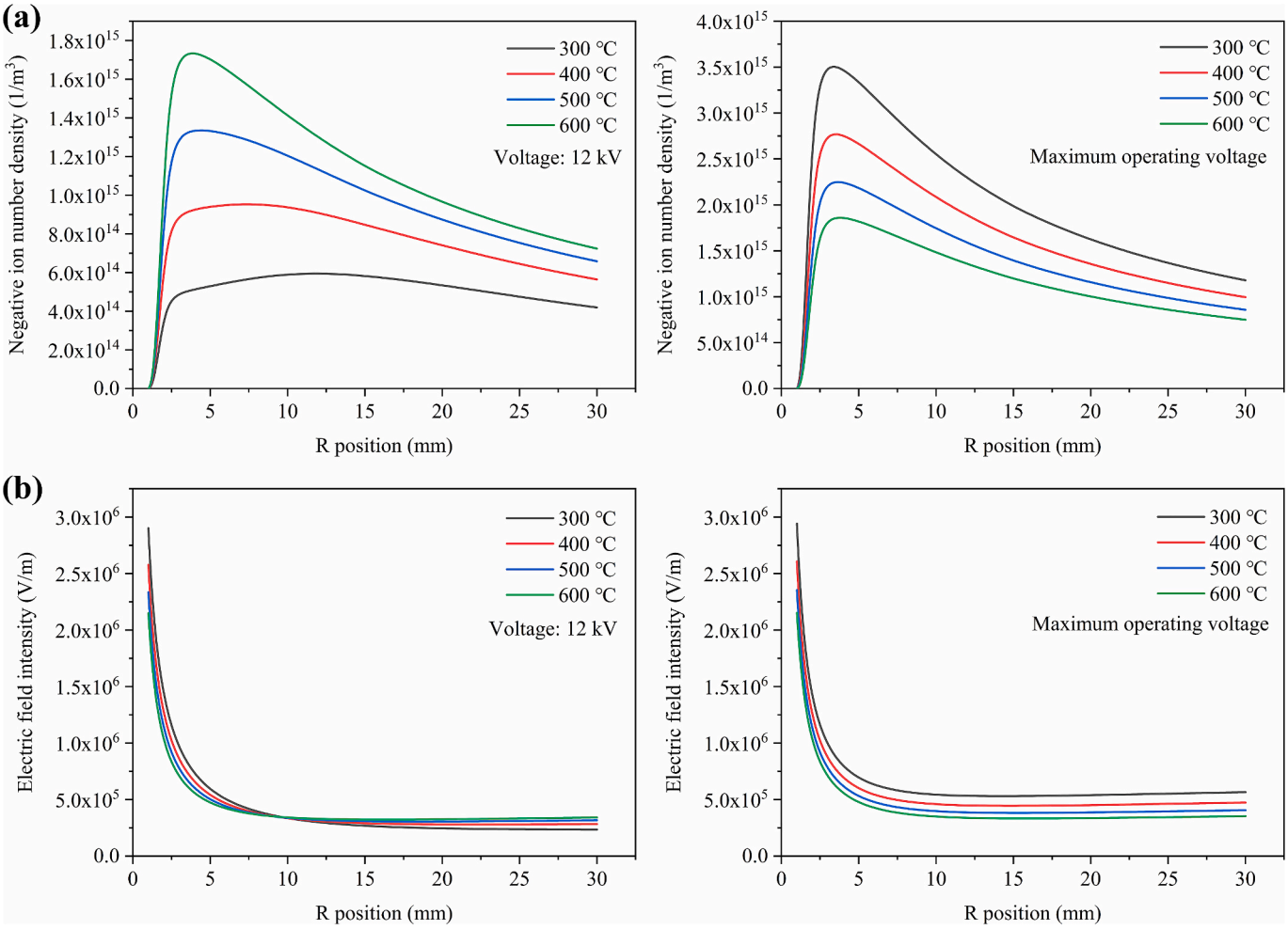

Fig. 10. Effect of temperature on (a) negative ion density and (b) electric field intensity at different given voltages.

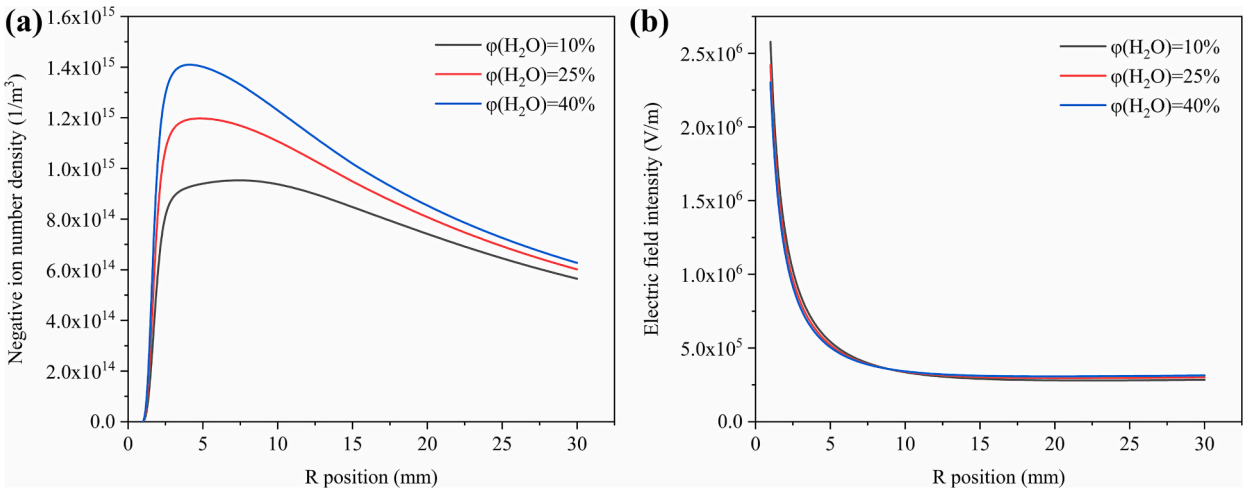

Fig. 11. Effect of H_2O volume fraction on the distribution of (a) negative ion density and (b) electric field intensity.

density and the charge time of particles, and there is no saturation value for the diffusion charge. Although the increase in temperature at the maximum operating voltage reduced the density of negative ions, it also decreased the migration velocity of small particles and increased their charge time, which led to an increase in the charge.

Fig. 14 shows the collection efficiency and migration velocity for particles with diameters of 0.8, 2, 4, and 6 μm at different temperatures under the same and maximum operating voltages. The relative collection efficiency η/η_0 (η_0 is the collection efficiency at 300 °C for particles with each diameter) was defined to compare the effect of temperature on the collection efficiency for particles with different diameters. The particle migration velocity, ω, was calculated using Deusch's formula:

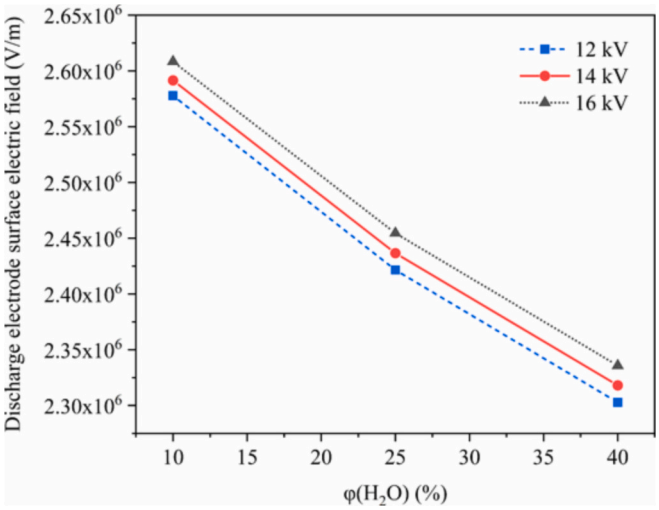

Fig. 12. Effect of H_2O volume fraction on the electric field intensity at the surface of the discharge electrode.

$$\omega = -\frac{Q}{A} ln(1-\eta) \tag{42}$$

where ω is the particle migration velocity, A is the area of the collection plate in the ESP, and Q is the gas flow rate in the ESP.

Fig. 14(a) shows the variation pattern of the dust removal efficiency and migration velocity with temperature at the same voltage. As can be seen from the figure, at the same voltage, increasing the temperature improved the dust collection efficiency, and the relative collection efficiency decreased with increasing particle size, indicating that this enhancement effect was more significant for small particles. In addition, the particle migration velocity increased with increasing temperature. From the previous analysis, it was clear that an increase in temperature at the same voltage mainly increased the negative ion density, thereby increasing the diffusion charge of the particles such that the collection efficiency increased with increasing temperature. In addition, the diffusion charge mainly acted on the small particles; therefore, the small particles were more affected by temperature at the same voltage. When the temperature increased from 300 °C to 600 °C, the collection efficiency of 0.8, 2, 4, and 6 μm particles increased from 14%, 17%, 27%, and 45% to 29%, 30.5%, 44%, and 65.5%, respectively, with improvements of 107%, 79%, 62%, and 45%, respectively.

Fig. 14(b) shows the variation pattern of the dust removal efficiency and migration velocity with temperature at the maximum operating voltage. At the maximum operating voltage, the collection efficiency and migration velocity decreased with increasing temperature, and the large particles were more significantly affected by temperature. This can

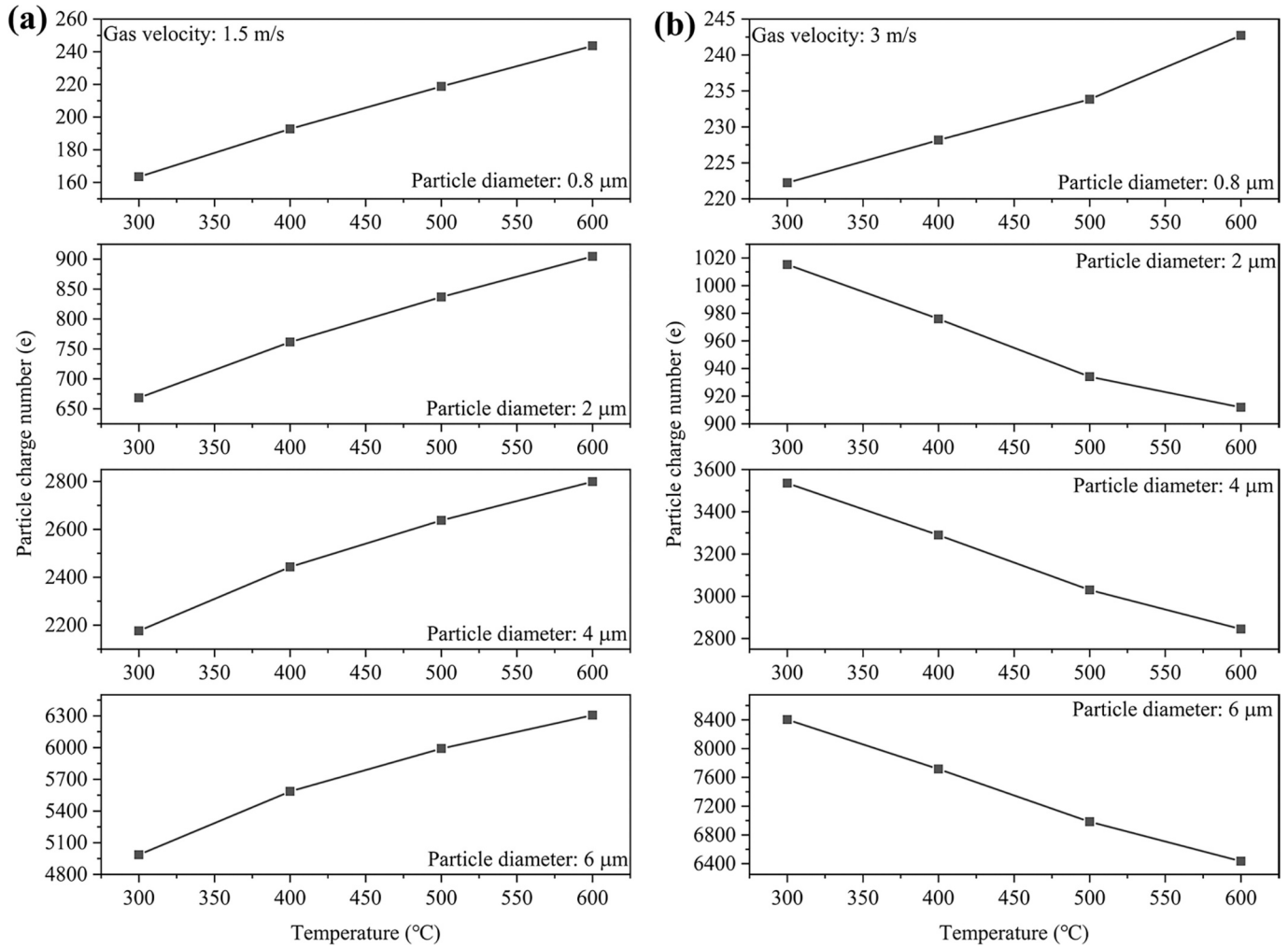

Fig. 13. Particle charge for particles with diameters of 0.8, 2, 4, 6 μm at different temperatures: (a)Voltage: 12 kV, (b) Maximum operating voltage.

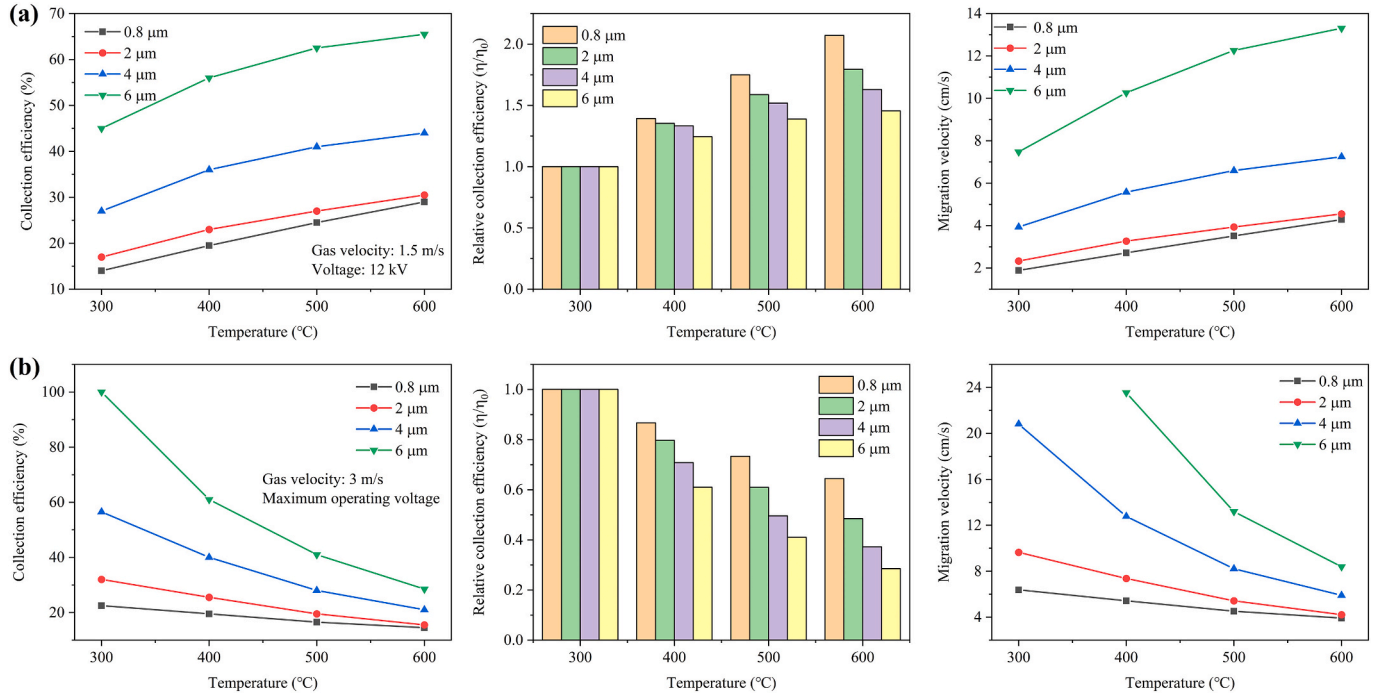

Fig. 14. Collection efficiency and migration velocity for particles with diameters of 0.8, 2, 4, 6 μm at different temperatures under (a) the same voltage (12 kV) and (b) maximum operating voltage.

be attributed to the fact that the high temperature reduced the maximum operating voltage of the ESP, causing both the negative ion density and electric field intensity to decrease with increasing temperature, resulting in the weakening of particle diffusion charging and electric field charging. In addition, diffusion charging was affected by both temperature and voltage, whereas electric field charging was affected only by voltage. For diffusion charging, an increase in temperature resulted in two opposite effects: On the one hand, an increase in temperature promoted ionization and increased the density of negative ions, which is beneficial for diffusion charging; on the other hand, the operating voltage decreased with increasing temperature, which decrease the density of negative ions and inhibited diffusion charging. Owing to the presence of these two mutually inhibiting effects, the weakening of the diffusion charge was relatively small, and thus, the small particles were less affected. Therefore, at the maximum operating voltage, the collection efficiency of the large particles was more sensitive to changes in temperature. When the temperature increased from 300 °C to 600 °C, the collection efficiency of 0.8, 2, 4, and 6 μm particles decreased from 22.5%, 32%, 56.5%, and 100% to 14.5%, 15.5%, 21%, and 28.5%, respectively, with reductions of 35.6%, 51.6%, 62.8%, and 71.5%, respectively. According to the above analysis, although increasing the temperature helped to improve the collection efficiency at the same voltage, the high temperature reduced the maximum operating voltage of the electric precipitator, which led to a decrease in the maximum collection efficiency. In actual industries, to obtain higher dust removal efficiencies, ESPs are expected to operate at higher voltages. Therefore, high temperatures are detrimental to the operation of ESPs overall, which is consistent with the experimental results of Xu et al. [1].

3.5.2. *Effect of H_2O concentration*

According to the previous analysis, increasing the H_2O concentration was conducive to increasing the negative ion density, which may be beneficial for electric dust removal. Therefore, we investigated the effect of different H_2O concentrations on the particle charge and collection efficiency. The relative particle charge q_p/q_{p0} (q_{p0} is the particle charge at 10% H_2O volume fraction) and the relative collection efficiency η/η_0 (η_0 is the collection efficiency at 10% H_2O volume fraction) were defined to compare the effects of H_2O concentration in flue gas on particle charge and collection efficiency.

Fig. 15 illustrates the charge of particles with diameters of 0.8 μm, 2, 4, and 6 μm at different H_2O volume fractions. When the volume fraction of H_2O increased, the particle charge increased, and the relative particle charge decreased with increasing particle diameter, indicating that increasing the H_2O concentration can enhance the particle charge, and this enhancement effect was more significant for small particles. When the volume fraction of H_2O increased from 10% to 40%, the charge of 0.8, 2, 4, and 6 μm particles increased from 192.7 e, 761.5 e, 2443.5 e, and 5585.7 e to 238.6 e, 890.8 e, 2766.5 e, and 6242.9 e, respectively, with increases of 23.7%, 17%, 13.2%, and 11.8%, respectively. From the previous analysis, it can be seen that increasing the H_2O concentration can significantly improve the density of negative ions, whereas the effect on the electric field strength is not significant. Therefore, increasing the H_2O volume fraction mainly enhanced the diffusion charge of particles, and the diffusion charge mainly acted on the charge process of small particles. Thus, increasing the H_2O concentration can improve the particle charge, and the improvement effect on small particles is more significant.

Fig. 16 shows the collection efficiency and migration velocity of particles with diameters of 0.8, 2, 4, and 6 μm at different H_2O volume fractions. As the volume fraction of H_2O in the flue gas increased, the collection efficiency and migration velocity of particles increased, and the relative collection efficiency decreased with increasing particle diameter, indicating that the collection efficiency of the small particles was more significantly influenced by the variation in the H_2O concentration. When the volume fraction of H_2O increased from 10% to 40%, the dust collection efficiencies of 0.8, 2, 4, and 6 μm particles increased from 19.5%, 23%, 36%, and 56% to 28%, 30%, 43%, and 65%, respectively, with improvements of 43.6%, 30.4%, 19.4%, and 16.1%, respectively. Therefore, increasing the H_2O concentration in high-temperature flue gas can improve the dust collection efficiency. During actual industrial operations, for high-temperature flue gas, the method of high-temperature water vapor conditioning can be used to improve the particle collection efficiency.

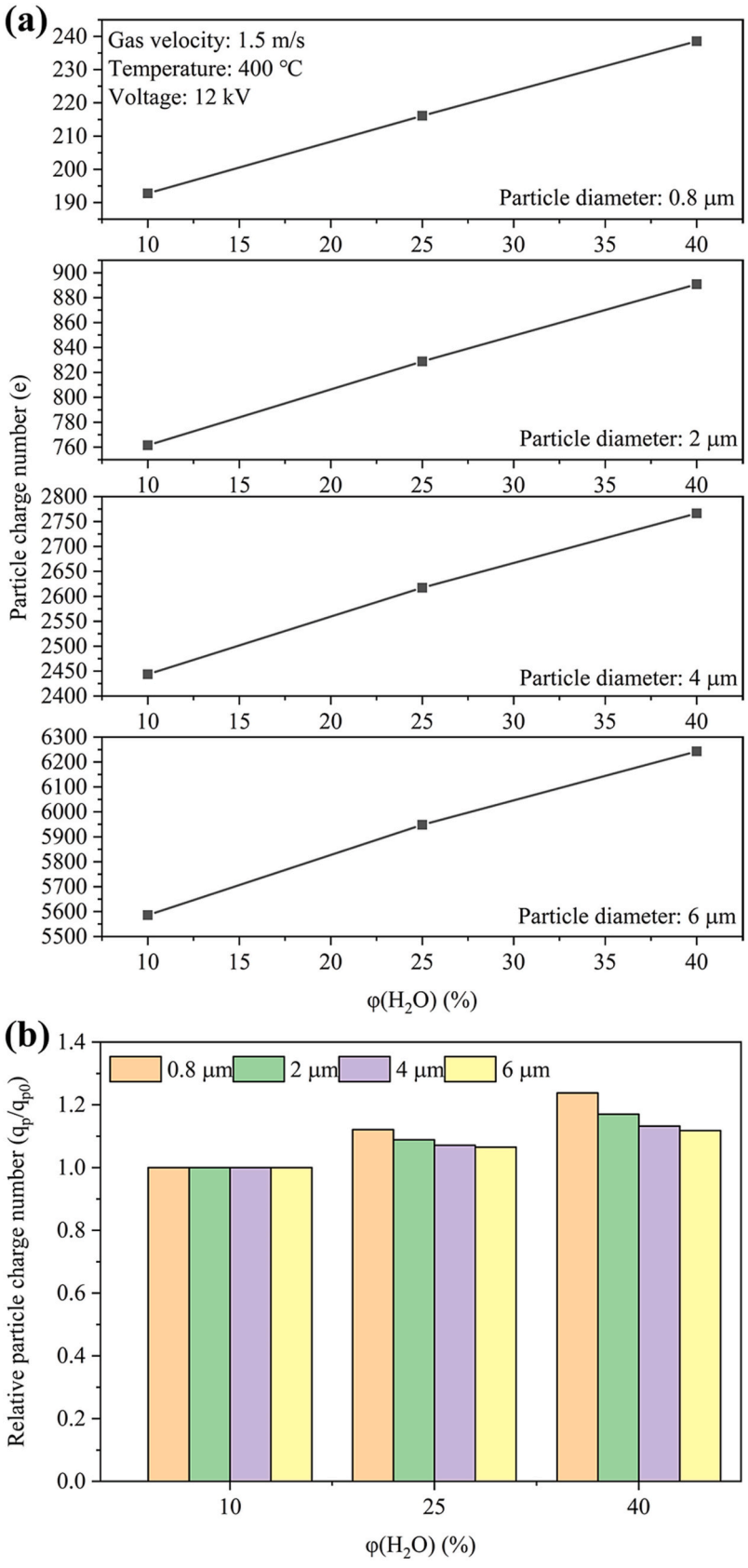

Fig. 15. Particle charge for particles with diameters of 0.8, 2, 4, 6 μm at different H_2O volume fractions.

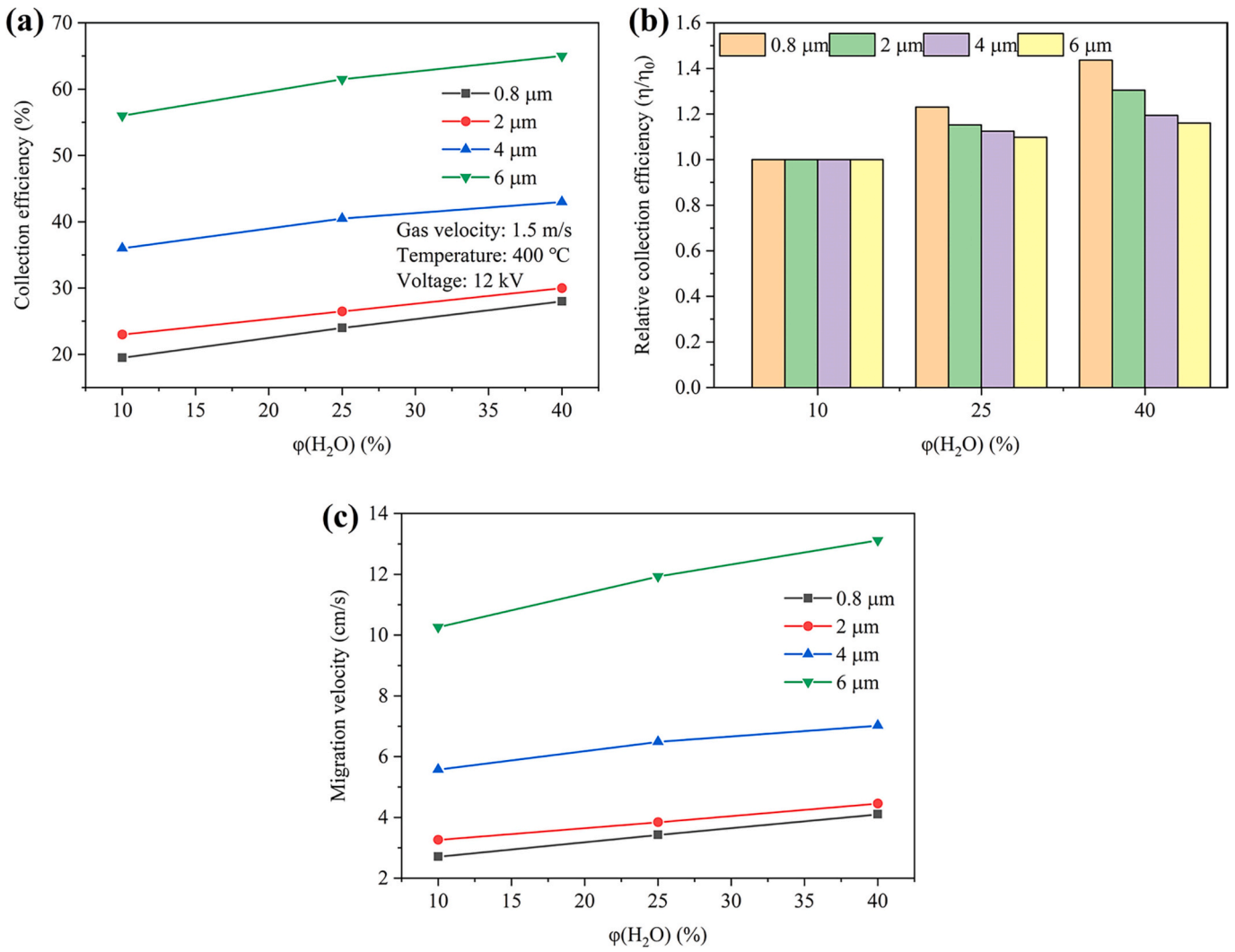

Fig. 16. Collection efficiency and migration velocity for particles with diameters of 0.8, 2, 4, 6 μm at different H_2O volume fractions.

4. Conclusions

In this study, an integrated mathematical model applicable to high-temperature ESP was developed using COMSOL Multiphysics, and the effects of temperature and H_2O concentration on ESP performance, such as the distribution of charge carriers, electric field characteristics, and the collection efficiency, were investigated. The main conclusions are summarized as follows:

(1) High-temperature corona currents consist of ion and electron currents. The electron current cannot be neglected during high-temperature gas discharge, whereas conventional corona discharge models usually adopt the assumption of neglecting electrons; therefore, conventional corona discharge models are not applicable to high-temperature corona discharge.

(2) At the same voltage, the negative-ion density increased with increasing temperature. With increasing temperature, the electric field intensity decreased in the area near the discharge electrode and increased in the area near the grounding electrode. At the maximum operating voltage, the negative ion density and electric field intensity decreased with increasing temperature because of the decrease in the maximum operating voltage with increasing temperature. It is unreasonable to use the constant value calculated using Peek's formula as the surface field intensity of the discharge electrode in the conventional corona discharge model because the surface field intensity changes with the change in voltage.

(3) Increasing the H_2O concentration in high-temperature flue gas can increase the electronegativity of the gas, thereby promoting the generation of negative ions and increasing the density of negative ions. The surface field intensity of the discharge electrode decreased with increasing H_2O concentration; however, the overall electric field intensity distribution was less affected by the H_2O concentration.

(4) At the same voltage, both the particle charge and collection efficiency increased with increasing temperature, and the effect of high temperature on the collection efficiency was more significant for small particles. At the maximum operating voltage, the electric field intensity and negative ion density decreased owing to the reduction in the maximum operating voltage caused by high temperature; therefore, the collection efficiency decreased with increasing temperature, and the decrease was greater for large particles. In actual industries, to achieve a maximum dust collection efficiency, ESPs are often operated at the maximum operating voltage; therefore, high temperatures are harmful to the operation of ESPs.

(5) The particle charge increased with increasing H_2O concentration in the high-temperature flue gas, and the charges of small particles were affected more by the H_2O concentration because the increase in H_2O concentration mainly increased the diffusion

charge of the particles. The collection efficiency increased with increasing H_2O concentration, and this enhancement effect decreased with increasing particle size. In actual industries, high-temperature water vapor can be used to condition high-temperature flue gas to improve the dust collection efficiency.

CRediT authorship contribution statement

Yongmin Shi: Conceptualization, Methodology, Investigation, Writing – original draft, Writing – review & editing. **Mengxiang Fang:** Funding acquisition, Writing – review & editing, Resources, Project administration. **Qinhui Wang:** Supervision, Resources. **Keping Yan:** Validation, Resources. **Jianmeng Cen:** Visualization, Resources. **Weiqiang Zeng:** Project administration. **Zhongyang Luo:** Supervision, Resources.

Declaration of Competing Interest

The authors declare that they have no known competing financial interests or personal relationships that could have appeared to influence the work reported in this paper.

Data availability

Data will be made available on request.

Acknowledgments

This work was supported by National Key Research and Development Program of China (2018YFB0605000).

Appendix A. Supplementary data

Supplementary data to this article can be found online at https://doi.org/10.1016/j.powtec.2022.117913.

References

[1] X. Xu, X. Gao, P. Yan, W. Zhu, C. Zheng, Y. Wang, Z. Luo, K. Cen, Particle migration and collection in a high-temperature electrostatic precipitator, Sep. Purif. Technol. 143 (2015) 184–191.
[2] M. Dong, F. Zhou, Y. Zhang, Y. Shang, S. Li, Numerical study on fine-particle charging and transport behaviour in electrostatic precipitators, Powder Technol. 330 (2018) 210–218.
[3] H. Bin, Z. Lin, Y. Yang, L. Fei, L. Cai, Y. Linjun, PM 2.5 and SO3 collaborative removal in electrostatic precipitator, Powder Technol. 318 (2017) 484–490.
[4] M. Ni, G. Yang, S. Wang, X. Wang, G. Xiao, C. Zheng, X. Gao, Z. Luo, K. Cen, Experimental investigation on the characteristics of ash layers in a high-temperature wire–cylinder electrostatic precipitator, Sep. Purif. Technol. 159 (2016) 135–146.
[5] K. Adamiak, Numerical models in simulating wire-plate electrostatic precipitators: a review, J. Electrost. 71 (2013) 673–680.
[6] Z. He, E.T.M. Dass, Correlation of design parameters with performance for electrostatic precipitator. Part I. 3D model development and validation, Appl. Math. Model. 57 (2018) 633–655.
[7] C. Zheng, X. Zhang, Z. Yang, C. Liang, Y. Guo, Y. Wang, X. Gao, Numerical simulation of corona discharge and particle transport behavior with the particle space charge effect, J. Aerosol Sci. 118 (2018) 22–33.
[8] G. Biskos, K. Reavell, N. Collings, Electrostatic characterisation of corona-wire aerosol chargers, J. Electrost. 63 (2005) 69–82.
[9] J. Anagnostopoulos, G. Bergeles, Corona discharge simulation in wire-duct electrostatic precipitator, J. Electrost. 54 (2002) 129–147.
[10] K. Luo, Y. Li, C. Zheng, X. Gao, J. Fan, Numerical simulation of temperature effect on particles behavior via electrostatic precipitators, Appl. Therm. Eng. 88 (2015) 127–139.
[11] D. Yang, B. Guo, X. Ye, A. Yu, J. Guo, Numerical simulation of electrostatic precipitator considering the dust particle space charge, Powder Technol. 354 (2019) 552–560.
[12] H. Zhang, L. Shao, W. Gao, Y. Wang, X. Liu, Y. Yang, C. Zheng, X. Gao, Particle charging in electric field under simulated SO3-containing flue gas at low temperature, FUEL 310 (2022), 122291.
[13] Y. Wang, H. Zhang, W. Gao, L. Shao, Z. Wu, Z. Zhao, C. Ge, D. Hu, C. Zheng, X. Gao, Improving the removal of particles via electrostatic precipitator by optimizing the corona wire arrangement, Powder Technol. 388 (2021) 201–211.
[14] W. Gao, Y. Wang, H. Zhang, B. Guo, C. Zheng, J. Guo, X. Gao, A. Yu, Effect of the Vortex formed by the Electrohydrodynamic flow on the motion of particles in a needle-plate electrostatic precipitator, Aerosol Air Qual. Res. 20 (2020) 2911–2924.
[15] B. Chen, Y. Guo, H. Li, B. Liu, Y. He, H. Zhao, Insights into the effect of the shape of collecting plates on particle precipitation processes in an electrostatic precipitator, J. Air Waste Manage. Assoc. 70 (2020) (1995) 892–903.
[16] G. Lee, S. Hwang, T. Cheon, H. Kim, B. Han, S. Yook, Optimization of pipe-and-spike discharge electrode shape for improving electrostatic precipitator collection efficiency, Powder Technol. 379 (2021) 241–250.
[17] W. Zhou, R. Jiang, Y. Sun, B. Chen, B. Liu, Study on multi-physical field characteristics of electrostatic precipitator with different collecting electrodes, Powder Technol. 381 (2021) 412–420.
[18] L. Liu, X. Gu, L. Zhang, T. Sun, Z. Cao, B. Yu, J. Li, L. Zhang, W. Xu, S. Bu, L. Zhang, Experiment and numerical simulation investigation on wire-plate electrostatic precipitator with expanded-shrunk spoilers, Powder Technol. 395 (2022) 60–70.
[19] A. Suriyawong, C.J. Hogan, J. Jiang, P. Biswas, Charged fraction and electrostatic collection of ultrafine and submicrometer particles formed during O2–CO2 coal combustion, Fuel 87 (2008) 673–682.
[20] T. Mikoviny, M. Kocan, S. Matejcik, N.J. Mason, J.D. Skalny, Experimental study of negative corona discharge in pure carbon dioxide and its mixtures with oxygen, J. Phys. D. Appl. Phys. 37 (2004) 64–73.
[21] H. Nouri, N. Zouzou, E. Moreau, L. Dascalescu, Y. Zebboudj, Effect of relative humidity on current–voltage characteristics of an electrostatic precipitator, J. Electrost. 70 (2012) 20–24.
[22] D. Dubois, N. Merbahi, O. Eichwald, M. Yousfi, M. Benhenni, Electrical analysis of positive corona discharge in air and N2, O2, and CO2 mixtures, J. Appl. Phys. 101 (2007), 053304.
[23] X. Wang, M. Ni, G. Xiao, J. Zhang, X. Gao, K. Cen, An analytical method for DC negative corona discharge in a wire-cylinder device at high temperatures, J. Electrost. 72 (2014) 270–284.
[24] G. Xiao, X. Wang, J. Zhang, M. Ni, X. Gao, K. Cen, Current analysis of DC negative corona discharge in a wire-cylinder configuration at high ambient temperatures, J. Electrost. 72 (2014) 107–119.
[25] A.V. Phelps. www.lxcat.net/Phelps, 2022 [2022-6-2].
[26] I.A. Kossyi, A.Y. Kostinsky, A.A. Matveyev, V.P. Silakov, Kinetic scheme of the non-equilibrium discharge in nitrogen-oxygen mixtures, Plasma Sources Sci. Technol. 1 (1992) 207–220.
[27] H. Hokazono, H. Fujimoto, Theoretical analysis of the CO2 molecule decomposition and contaminants yield in transversely excited atmospheric CO2 laser discharge, J. Appl. Phys. 62 (1987) 1585–1594.
[28] S.R. Sun, H.X. Wang, A. Bogaerts, Chemistry reduction of complex CO2 chemical kinetics: application to a gliding arc plasma, Plasma Sources Sci. Technol. 29 (2020) 25012.
[29] D.X. Liu, P. Bruggeman, F. Iza, M.Z. Rong, M.G. Kong, Global model of low-temperature atmospheric-pressure He + H2O plasmas, Plasma Sources Sci. Technol. 19 (2010), 025018-1/22.
[30] S.D. Shandakov, A.G. Nasibulin, E.I. Kauppinen, Phenomenological description of mobility of nm- and sub-nm-sized charged aerosol particles in electric field, J. Aerosol Sci. 36 (2005) 1125–1143.
[31] S. Xu, Direct calculation method of flue gas properties, J. Suzhou Inst. Silk Textile Technol. (1999) 32–36.
[32] P.A. Lawless, Particle charging bounds, symmetry relations, and an analytic charging rate model for the continuum regime, J. Aerosol Sci. 27 (1996) 191–215.
[33] A. Villot, Y.F.J. Gonthier, E. Gonze, A. Bernis, Numerical model of current–voltage curve for the wire-cylinder electrostatic precipitators in negative voltage in the presence of nonpolar gases, IEEE Trans. Plasma Sci. 38 (2010) 2031–2040.
[34] Q. Chen, M. Fang, J. Cen, Y. Zhao, Q. Wang, Y. Wang, Electrostatic precipitation under coal pyrolysis gas at high temperatures, Powder Technol. 362 (2020) 1–10.
[35] M. Goldman, A. Goldman, R.S. Sigmond, The corona discharge, its properties and specific uses, Pure Appl. Chem. 57 (1985) 1353–1362.
[36] R.S. Sigmond, Simple approximate treatment of unipolar space-charge-dominated coronas: the Warburg law and the saturation current, J. Appl. Phys. 53 (1982) 891–898.
[37] P. Yan, C. Zheng, G. Xiao, X. Xu, X. Gao, Z. Luo, K. Cen, Characteristics of negative DC corona discharge in a wire–plate configuration at high temperatures, Sep. Purif. Technol. 139 (2015) 5–13.
[38] Q. Chen, M. Fang, J. Cen, J. Liu, Characteristics of negative DC discharge in a wire-cylinder configuration under coal pyrolysis gas components at high temperatures, RSC Adv. 8 (2018) 22737–22747.
[39] Y. Feng, W. Gao, M. Zhou, K. Luo, J. Fan, C. Zheng, X. Gao, Numerical modeling on simultaneous removal of mercury and particulate matter within an electrostatic precipitator, Adv. Powder Technol. 31 (2020) 1759–1770.
[40] D. Wang, Q. Jing, X. Qian, M. Yuan, C. Shi, Influence research of electrostatic environment on dispersion and explosion characteristics of typical biomass organic dust clouds, Powder Technol. 404 (2022), 117444.